





## Article

# Fluid–Structure Interaction Modeling of Structural Loads and Fatigue Life Analysis of Tidal Stream Turbine

Yuquan Zhang <sup>1,2</sup>, Zhiqiang Liu <sup>1</sup>, Chengyi Li <sup>2,\*</sup>, Xuemei Wang <sup>3</sup>, Yuan Zheng <sup>1</sup>, Zhi Zhang <sup>2</sup>, Emmanuel Fernandez-Rodriguez <sup>4</sup> and Rabea Jamil Mahfoud <sup>2</sup>

<sup>1</sup> College of Energy and Electrical Engineering, Hohai University, Nanjing 210098, China

<sup>2</sup> College of Water Conservancy and Hydropower Engineering, Hohai University, Nanjing 210098, China

<sup>3</sup> Chongqing Jiangjin Shipbuilding Industry Co., Ltd., Chongqing 402263, China

<sup>4</sup> Technological Institute of Merida, Technological Avenue, Merida 97118, Mexico

\* Correspondence: lichengyi@hhu.edu.cn

**Abstract:** Developing reliable tidal-energy turbines of a large size and capacity links to preservation of the structural safety and stability of the blades. In this study, a bidirectional fluid–structure coupling method was applied to analyze the hydrodynamic performance and structural characteristics of the blade of a tidal-stream turbine. Analyses were conducted on the transient and stable structural stresses, fatigue, and deformations under the influence of water depth and turbine rotational speed. The performance predictions with and without fluid–structure coupling are similar to measurements. The water-depth change has little effect on the stress and deformation change of the blade, while the turbine-speed change has the most significant effect on it. When the turbine just starts, the blade will be subject to a sudden change load. This is due to the increase in turbine speed, resulting in the sudden load. Similar to the trend of blade stress, the blade safety factor is lower near the root of the blade, and the turbine-speed change has a more significant impact on the blade structure's safety. However, the number of stress cycles in the blade at different rotational speeds is within the safety range.

**Keywords:** tidal stream turbine; CFD; fatigue life; fluid–structure interaction; blade safety factor

**MSC:** 76E07



**Citation:** Zhang, Y.; Liu, Z.; Li, C.; Wang, X.; Zheng, Y.; Zhang, Z.; Fernandez-Rodriguez, E.; Mahfoud, R.J. Fluid–Structure Interaction Modeling of Structural Loads and Fatigue Life Analysis of Tidal Stream Turbine. *Mathematics* **2022**, *10*, 3674. <https://doi.org/10.3390/math10193674>

Academic Editors: Zhuojia Fu, Yiqian He and Hui Zheng

Received: 30 August 2022

Accepted: 29 September 2022

Published: 7 October 2022

**Publisher's Note:** MDPI stays neutral with regard to jurisdictional claims in published maps and institutional affiliations.



**Copyright:** © 2022 by the authors. Licensee MDPI, Basel, Switzerland. This article is an open access article distributed under the terms and conditions of the Creative Commons Attribution (CC BY) license (<https://creativecommons.org/licenses/by/4.0/>).

## 1. Introduction

Environmentalists emphasize the imminent animal- and human-habitat disruption from the rising climate temperatures due to the large-scale implementation and burning of fossil fuels. Attempts to reverse the ecological damage are without economical side effects and comprise the carbon residues' elimination and the minimization and eventual substitution of fossil-based systems into renewable power systems. However, the strategy carries obstacles, such as overcoming renewable discontinuous power output, equalizing cost disparities, and improving reception among users. More recently, supporters have stressed the importance of combining renewable resources, named hybrid systems, to achieve economy of scale and solve the cost-inefficient energy accumulators. Tidal-stream energy fits into this concept. It is a high-density, unrenowned, and foreseeable source, and it could supplement wind offshore systems, once viable. The popular mode for current kinetic energy conversion is through rotary machines (three-bladed turbines) stationed in the sea bottom and coupled to electrical generators. Due to its parallelism to offshore wind, the blade profile can be selected to achieve power efficiencies of 48% but may be more in bounded conditions; this is presumed from the multi-member concept and relatively large sweep to incident channel area.

Relevant inquiries, nevertheless, are whether the underwater devices can survive the corrosivity and unexpected sea environments, as well as where they can live up to

investors' expectations to deliver large low-cost energy over a reasonable time. Since direct field testing is difficult, scientific strategies involve the artificial flow replication, to comprehend the alone and multi-turbine operation, and possible interference in the aquatic life. However, as sites diverge in bathymetry and geographical position, caution in regard to the measured properties must be applied; the current may prompt turbine blockage effects due to shallow depth and mix with omni-directional waves, and the turbulence intensity (TI) can be small (0.1) or critical (0.4), whilst the shear may or not exemplify power laws.

Contrary to uniform flows, the turbine's fluctuating performance is intricate, and thus, the association is unclear between the dynamic blade effects and the main properties of the turbulence and with waves. Tidal-energy turbines are generally arranged in complex marine environments with high flow velocities [1,2]. So, the research methods for tidal-energy turbines are mainly model tests and numerical simulations [3–7]. Allmark et al. [8] conducted model tests of a tidal-energy turbine with a model scale of 1:20 in a recirculating water tank. They found that by using the upstream region of the turbine to achieve acceleration, the turbine could achieve higher power, and the control scheme used had a significant effect on power and load fluctuations. Myers et al. [9] conducted model experiments in a circulating water tank with a turbine diameter of 0.4 m and a ratio of 1:30 and found that, as the inlet flow rate increases, it increases the turbulence around the runner and the change in water-surface height. Zhang et al. [10] evaluated the wake characteristics of a turbine under wave action and showed that the presence of waves has an effect on the intensity of vorticity and turbulence in the near wake field. Gaurier et al. [5] studied load fluctuations in a tank for a turbine model with a scale of 1:20 and showed that fluctuations in turbine load respond directly to fluctuations in low-frequency velocities and are influenced by turbulence shedding from the turbine. This provides substantial suggestions for conducting further fatigue analyses for turbine conditions with high Reynolds-number flow.

Numerical simulations have gradually become a convenient and credible research method through the continuous validation of model experiments conducted by researchers [11]. Tian et al. [12] used available experimental data to verify the reliability of the adopted calculation method, and based on this, the effects of the yaw angle and turbulence-intensity drops on the performance of a horizontal axis tidal energy turbine with a diameter of 3 m were calculated. The results showed that the effects of different turbulence intensities on power coefficient ( $C_p$ ) and thrust coefficient ( $C_t$ ) are small, but the effects on wake are large. Ahmadi et al. [13] and others studied the evolution of the wake characteristics of horizontal-axis tidal-energy turbines experimentally, followed by numerical simulations of the flow field, using a combination of Large Eddy Simulation (LES) and Augmented Lagrangian Method (ALM) to partition the turbine wake into different regions, suggesting that to study the characteristics of the turbine wake, it is necessary to understand the variation of flow characteristics in the transition zone.

With the development of tidal-energy turbines to large capacity and large size, their structural safety and stability have received more and more attention [14–17]. On the one hand, the horizontal-axis tidal turbine will produce hydroelastic deformation under the action of water flow, and the deformation produced by the blades will also act on the water flow to produce a certain impact on the flow field; on the other hand, compared with the wind turbine, the tidal turbine will be subject to greater thrust due to the density of seawater [18]. Therefore, the study of fluid–structure coupling for tidal-energy turbines has also attracted the attention of experts and scholars. At present, many scholars have started to conduct fluid–structure coupling analysis on tidal turbines, mainly focusing on their structural reliability, and then achieved the purpose of optimizing the blades.

Some researchers have analyzed the structural performance of tidal turbine blades under different conditions by using the unidirectional fluid–structure coupling method [19]. Hafeez et al. [20] investigated the effect of the velocity shear on the performance and structure of the tidal turbine, comparing the blade deformation in uniform flow and

shear flow, and found that the blade deformation of the turbine under velocity shear flow changed significantly. Liu et al. [21] analyzed the structural performance of blades made of stainless steel and structural steel at different rotational speeds, and the results showed that the output power of the turbine was lower at low rotational speeds, but the energy gain efficiency was higher, and the blades of both materials met the structural safety requirements. Ullah et al. [22], on the other hand, performed a fatigue-life analysis and modal analysis of the hydraulic turbine. Some scholars have also used a bidirectional fluid–structure coupling approach in order to obtain the transient structural response of the blades [23–25]. Nicholls-Lee et al. [26] developed an adaptive composite blade design tool and performed a bidirectional fluid–structure coupling analysis on a series of composite bending–torsion coupled blades, and the results showed that practical design of a properly designed blade can achieve a 12% reduction in thrust coefficient and an effective 5% increase in power coefficient. Badshah et al. [27] showed that the difference between CFD calculation results and fluid–structure coupling calculation results is less than 10%, and the two calculation conditions differ in the results of the blade-surface pressure difference. Tatum et al. [28] recognized that wave action would cause the hydraulic turbine’s asymmetric loading, so the turbine characteristics were calculated for uncoupled CFD and bidirectional fluid–structure coupling conditions, and the comparison revealed no significant difference between the two calculations; this is a matter of blade-material selection. Khalid et al. [24] simulated the transient structural response of a vertical axis tidal-energy turbine runner, using the fluid–structure coupling method; the blade deformation at each time step was considered in the calculation, and a new calculation method was proposed: transferring the file in ANSYS-APDL to obtain the solution results.

Clearly, an implication of turbine (performance curve and number of blades) and flow operation (turbulence profile) and design (vertical vs horizontal), along with the model differences, raises important questions about the generalizability of the above numerical findings. Therefore, in this study, the hydrodynamic performance and structural characteristics of the turbine were numerically simulated and analyzed based on the bidirectional fluid–structure coupling calculation, and the accuracy of the calculation results was verified by model tests. The prototype is a standard three-bladed horizontal-axis concept, operating in a flow with a turbulence intensity of 7%, and depth variation resembling the logarithmic power law. The fatigue life of the blade was also predicted by considering the influence of the turbine speed and water-depth-variation factors. Our work provides a reference for the design and material application of the blade of the tidal-energy turbine. In our view, these results represent an excellent initial step toward the wider use of the Coupled Fluid Structure model due to high computational accuracy and resource efficiency, as well as further testing in more complex situations, such as incoming waves and currents, and floating turbine systems.

## 2. Basic Theory

The fluid–structure coupling models the complex interaction between the turbine and water by first treating separately and then coupling the behavior of the incompressible fluid (water) and deformable structure. The strategy has been used to contemplate complex physical phenomena, such as smoking, and can benefit by the use of advanced backed-up separate solvers, applicable to the matter and operating state. Parameters in the method’s stability, resource and time requirement, and preciseness comprise the mode and mechanisms of fluid–structure data (interface) communication. If the governing equations of the fluid and structure both satisfy, per time-step calculation, the coupling is said to be strong. The integrated equation is as follows:

$$\begin{bmatrix} A_{FF} & A_{FS} \\ A_{SF} & A_{SS} \end{bmatrix} \begin{bmatrix} \Delta X_F^K \\ \Delta X_S^K \end{bmatrix} = \begin{bmatrix} B_F \\ B_S \end{bmatrix} \quad (1)$$

where  $A_{FF}$  is the fluid domain coefficient matrix,  $\Delta X_F^K$  is the physical solvable quantity,  $B_F$  is the external force, and  $K$  is the number of time iteration steps; the subscripts  $F$  and  $S$

refer to the fluid and solid domain, respectively whilst  $A_{SF}$  and  $A_{FS}$  are both fluid–structure coupling matrices.

Theoretically, the strong coupling lacks time lag, and the solution’s stability, visualization, and accuracy are high. However, the iterative process in the interface becomes time and resource exhaustive, especially for three-dimensional natural-phenomena problems. An alternative to maximize resource efficiency is to satisfy the interface’s governing equations, only once per time step, called weak coupling; however, it carries well-known defects: instabilities in strong added-mass circumstances and in solutions, confining the time-step calculation. Additionally, the data transfer between the fluid and the solid modules can be unidirectional, reducing complexity, or reciprocal by assuming the solid deformations alter the surrounding flow, as in the blade against the incident current. The structural dynamics equations of the two-way coupling is as follows:

$$[M]\{x''\} + [C]\{x'\} + [K]\{x\} = \{F(t)\} \quad (2)$$

where the matrix,  $[M]$ , is the mass;  $[C]$  is the damping; and  $[K]$  is the stiffness. Moreover, the vector of displacement is  $\{x\}$ , that of force is  $\{F(t)\}$ , that of velocity is  $\{x'\}$ , and that of acceleration is  $\{x''\}$ .

The following conditions are satisfied for data exchange at the relevant fluid–structure coupled intersection:

$$\begin{cases} u_{s,f} = u_{f,s} \\ v_{s,f} = v_{f,s} \end{cases} \quad (3)$$

where  $u$  is the normal-phase displacement component, and  $v$  is the normal-phase velocity component.

### 3. Computational Model

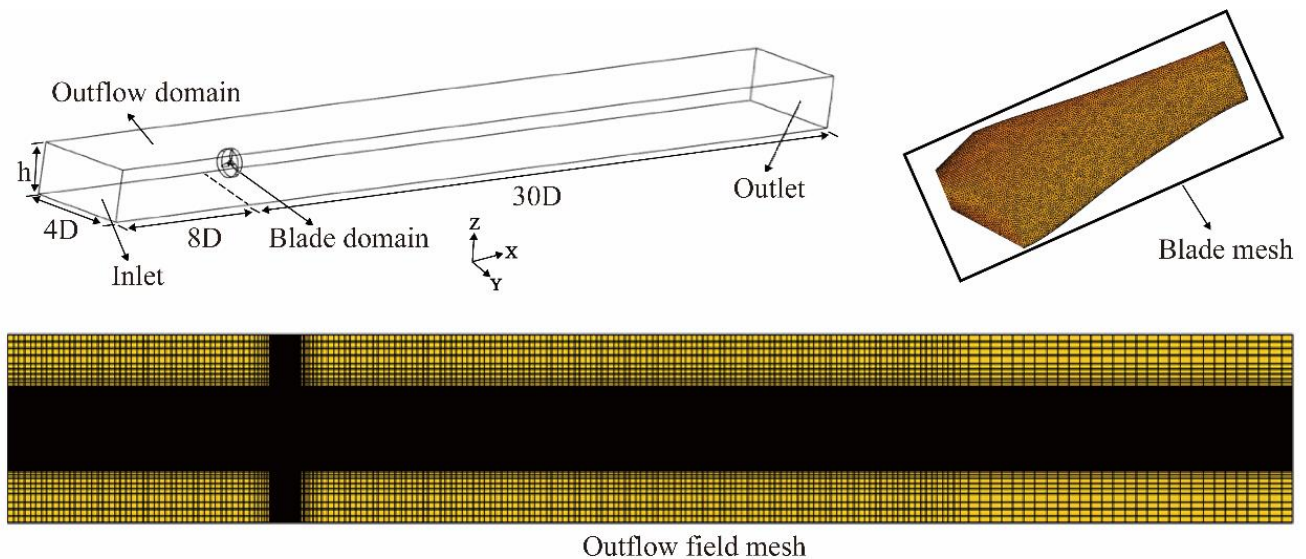
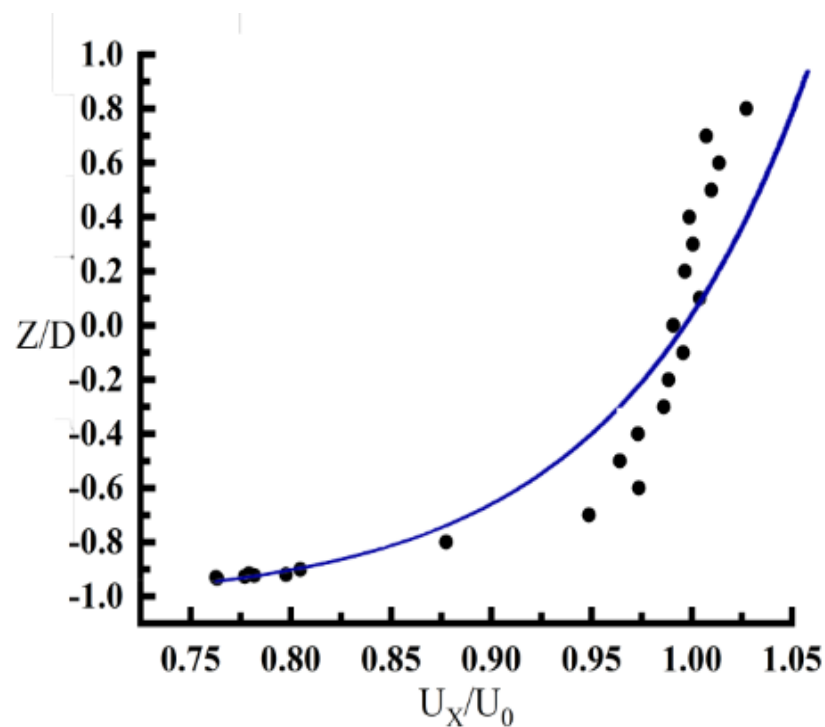
#### 3.1. Numerical Calculation Model

A bidirectional weak coupling fluid–structure model, the ANSYS Workbench platform Fluent, Transient Structural and System Coupling, simulates the turbine transient responses due to incident turbulent current. The CFD-based model is divided into two domains: the blade domain of radius 0.15 m ( $D/2$ ), and a rectangular prism comprising the outflow field. The width of the prism is set to  $4D$ , consistent with the channel’s width, whilst the water depth is set to  $h = [1.6D, 2D, 2.4D]$  in order to capture the channel blockage effects on the wake and turbine development. The blade hub is at half-water depth,  $8D$  from the upstream inlet and  $30D$  from the downstream outlet. The blade material is set to Aluminum 6061, with properties summarized in Table 1. To acquire a consistent mesh around the complex blade geometry by virtue of the radial angle variation, the tetrahedral grids are used for the blade domain, with blade sections locally encrypted to increase the result accuracy. The boundary-layer grid is set for the blade boundary, and the height of the first-layer grid is 0.02 mm. The hexahedral grid, known for yielding higher accuracy, distortion resistance, and the number of divided grids, is used for the outflow field. In order to further reduce the influence of the outflow field calculation, the blade domain is encrypted, and the final grid structure is divided as shown in Figure 1. The eddy-viscosity model, SST  $k-\omega$ , accounts for turbulent shear stresses. The solution of the Navier–Stokes (NS) equations incorporates an implicit scheme. The convective components are discretized with second-order upwind schemes, owing to good convergence and stability features. The pressure–velocity linkage in the NS equation is resolved iteratively via the SIMPLE algorithm. The velocity depth variation is close to the logarithmic power law, as shown in Figure 2. The fitting formula is as follows:

$$V = 0.023 \ln \left( \frac{z}{0.0015} + 57.7 \right) + 0.25 \quad (4)$$

**Table 1.** Material properties of 6061 aluminum.

Material	Density ( $\text{kg}\cdot\text{m}^{-3}$ )	Young's Modulus (Pa)	Poisson's Ratio
Aluminum 6061	2750	$7\text{e} + 10$	0.33

**Figure 1.** CFD model and the division of the mesh.**Figure 2.** Vertical velocity distribution.

The mean velocity across the swept area is  $0.4\text{ m/s}$ , with a turbulence intensity of 7%. Consequently, the boundary condition at the inlet is the velocity inlet, and the velocity varies according to Equation (4), whereas at the pressure outlet, the relative atmospheric pressure is set to 0. The free liquid surface is set to symmetry, and the moving mesh is used for the non-constant solution of the fluid domain. Figure 1 shows the mesh structure and main characteristics of the domains.



The solid domain part uses a tetrahedral mesh. The radial and axial displacement constraints are applied to the blade structural body. Gravity is present, and the blade surface is the fluid–structure coupling intersection. The constraints and mesh domain of the solid part are shown in Figure 3.

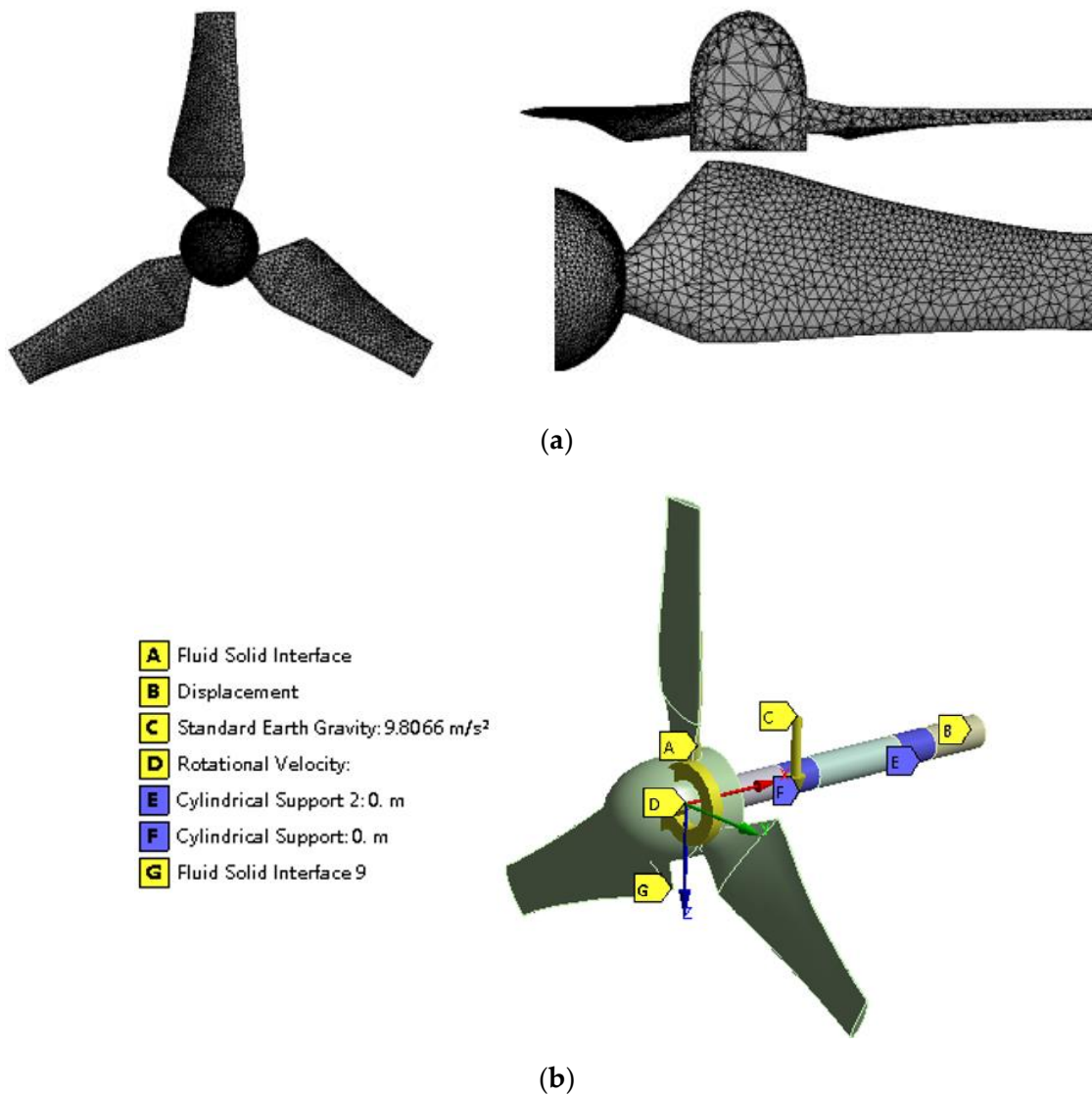


**Figure 3.** Mesh division and constraint setting of solid domain model: (a) mesh of solid domain and (b) constraints on solid domain.

### 3.2. Grid-Independence Verification

A grid-independence test investigates the method's computational resource with result accuracy. For the fluid domain, the grid number ranges from 3.5 to 7 million, whereas in the solid, the unidirectional fluid–structure coupling uses a grid size of 2 to 6 mm. The water depth is set to 0.6 m, with a blade angular speed of 100 r/min. As shown in Figure 4 and Table 2, the  $C_p$  and  $C_t$  values quickly decrease from 4.5 to 6 million grids, and then asymptote with numbers over 6 million. The maximum deformation and stress increases with grid reduction and converges with sizes less than 4 mm. Consequently, using a grid size of 3 mm for the solid and 6 million grids for the fluid saves computational resource without sacrificing accuracy level ( $<0.1\%$ ). The bidirectional fluid–solid coupling simulation was conducted by a computer with 32-cores AMD CPU. The final computation time for each case is 132 h.

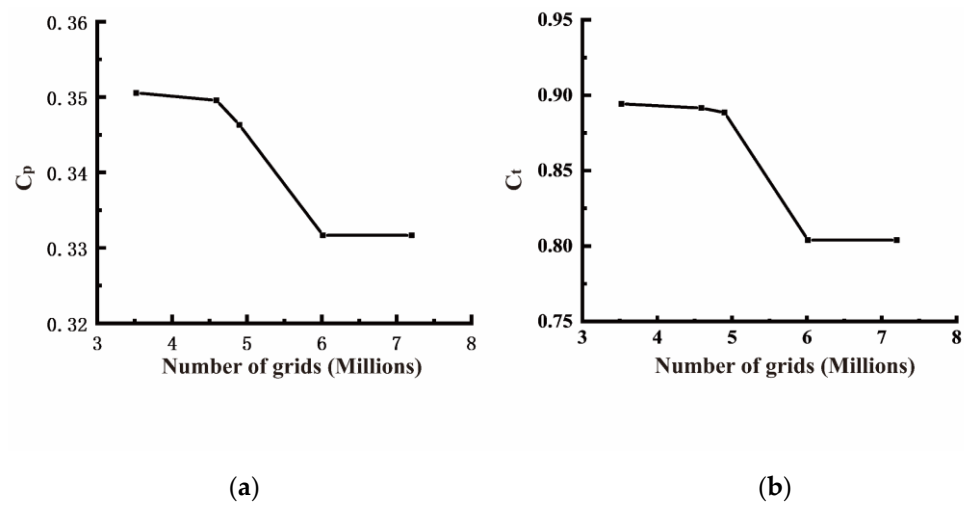


**Figure 4.** Grid-independence verification of fluid domain: (a)  $C_p$  and (b)  $C_t$ .

**Table 2.** Grid-independent verification of solid domains.

Segmentation Scheme	Grid Size (mm)	Number of Grids	Maximum Deformation (m)	Maximum Stress (MPa)
1	6	4187	0.012049	979.2
2	5	6409	0.012191	984.68
3	4	9616	0.012376	1122.3
4	3	15,337	0.012614	1307.5
5	2	43,382	0.012691	1337

### 3.3. Model Test Validation

The power output of the modeled 3-bladed turbine was examined in the hydrodynamic laboratory of Shandong Transportation Institute, using a flume of 50 m in length, 1.2 m in width, and 1.2 m in depth. The pumped water recirculates from the upstream inlet to the downstream via a returning underneath chamber, and the water depth ( $h$ ) is 0.6 m. The piled turbine is suspended in a metal cage, confining the speed and torque controller and electric cables. This is then fixed by using a crossbeam on the flume, allowing for the adjustment of the hub height (0.3 m). Figure 5 presents the experimental setup.

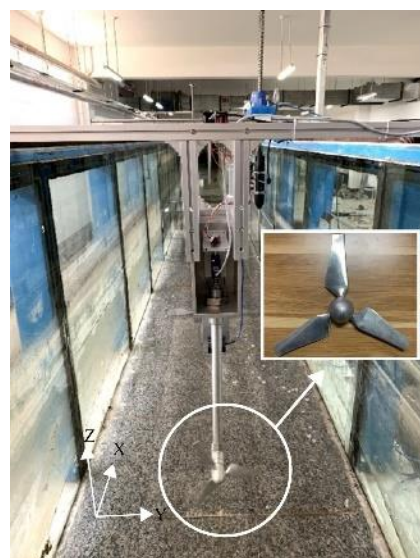


**Figure 5.** Layout of circulation pool and turbine.

Figure 6 shows the comparison of results calculated by the FSI method and regular CFD method with the experimental results of the current study. As seen, the predicted power coefficients by BEMT, FSI, and CFD follow an inverted u-curve with a tip-speed ratio (TSR) of  $TSR = \omega R/U$ , culminating at  $TSR = 3.9$ , with  $C_p = 0.332$ – $0.345$ . In general, the FSI simulations deviate more from the measurements than the CFD's do due to the non-optimal initial twist blade angle and deformation consideration; however, the error is less than 4.01% for the contemplated study's range ( $TSR = 3.64$ – $4.32$ ).

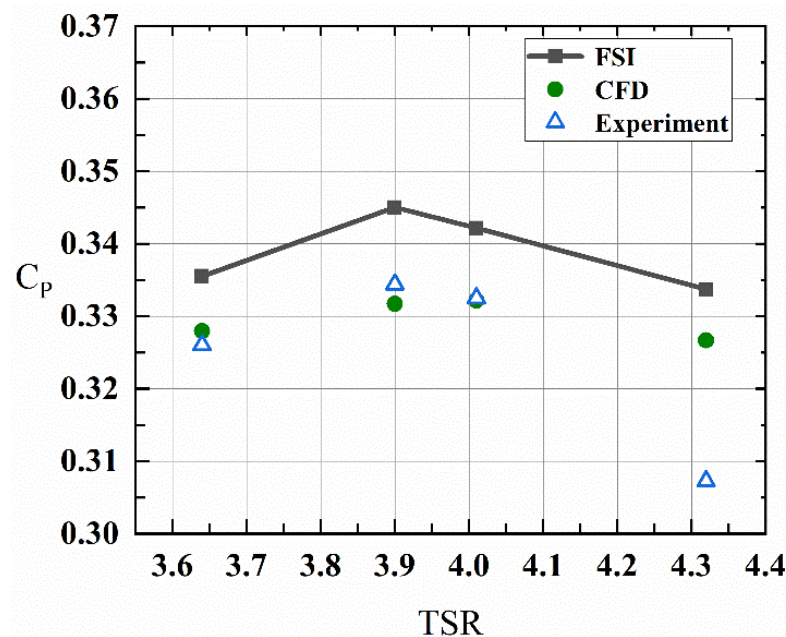


Figure 6. Graph of  $C_p$  with TSR.

#### 4. Results Analysis

##### 4.1. Hydrodynamic Performance of Blades

As Figure 7 demonstrates, the pressure simulations follow S-shaped curves, with upper asymptote (near the root) stretching further and lower (at the tip) shifting downwardly with radial distance. This behavior is attributed to two issues: a larger power section performance, apart from the blade root, augmenting the low–high pressure ranges; and the closer cavitation occurrence at the wingtip due to high tangential velocity ( $\omega \cdot r$ ). The only observable simulation difference is at the rear of the blade; it is slightly more negative with than without the fluid–structure coupling condition, due to a small deformation of the blade.

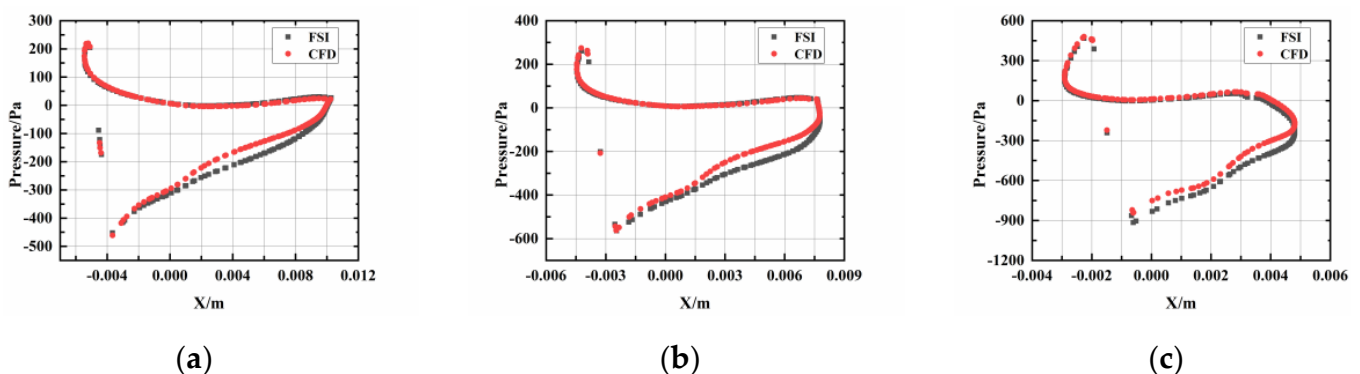
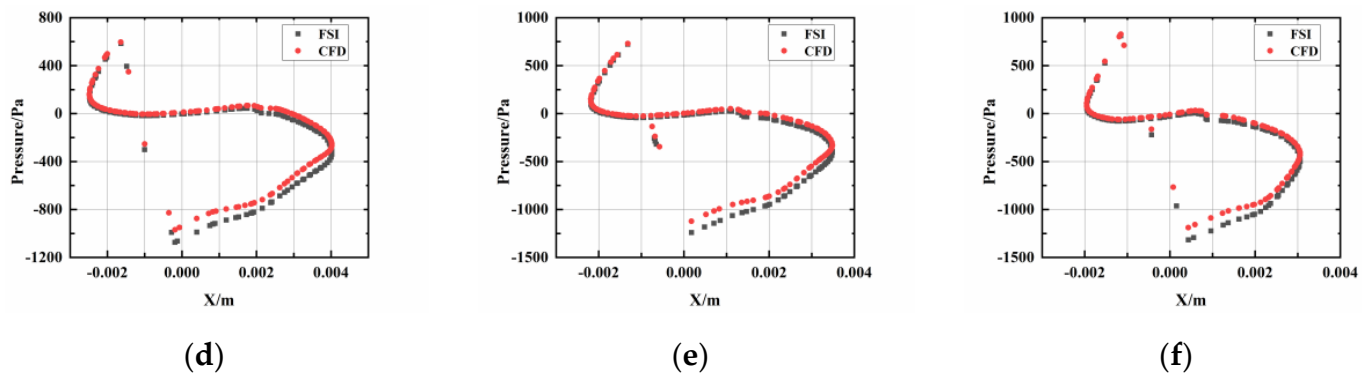


Figure 7. Cont.





**Figure 7.** Pressure distribution of different blade sections: (a) span = 20%, (b) span = 40%, (c) span = 50%, (d) span = 60%, (e) span = 70%, and (f) span = 80%.

#### 4.2. Blade Structural Stress Analysis

The structural characteristics of the blade were analyzed for a water depth of 0.6 m, an installation height of 0.3 m, and a turbine speed of 100 r/min under fluid–structure coupling conditions. The operation of the tidal-energy turbine for 3 s is calculated, and Figure 8 shows the dynamic stress distribution of the turbine blades at different times. It can be seen that the stress features similar lanceolate contours per blade, extending from the mid-root to almost all the blade, and reducing in intensity radially, reminiscent of an enlarged flame-like shape. Over time, the inner-core strength slightly augments and extends radially. This is because the blade is fixedly connected to the hub, and the blade can be regarded as a cantilever beam, and the bending moment and shear force near the blade root are maximum under the action of fluid loads, such as water thrust. The trend of the stress distribution on the three blades of the blade under each moment is that the maximum stress is at the root of the blade and decreases with an elliptical gradient toward the tip of the blade. When the blade starts to operate, the maximum stress on its surface rises rapidly, with the maximum value reaching 0.596 MPa, and the large stress-distribution area expands rapidly. As the turbine operation gradually stabilizes, the blade’s stress distribution is basically similar, and the maximum stress fluctuates in a small range, which is the result of the alternating cyclic load on the blade.

Figure 9 shows the deformation distribution of the blade at different moments. It can be clearly seen that the deformation of the blade’s surface at each moment is gradually increasing from the root to the tip of the blade. Combined with Figure 8, it can be found that the maximum blade deformation increases equally rapidly when the turbine is first started and fluctuates in a small range subsequently, due to the stable operation of the blade.

Figure 10 shows the variation of the maximum blade stress with time for 3 s operation under the water depth of 0.48 m, 0.6 m, and 0.72 m operating conditions. From the curves in the figure, it can be seen that the stress initially features an abrupt inverse u-curve before stabilizing, though in a fluctuating manner. The water depth reduces moderately the transient peak but slightly the stable stress. The maximum stress changes in all three water depth conditions show similar small amplitude periodic fluctuations. The turbine is operated under the maximum blocking ratio at the water depth of 0.48 m, and the maximum stress of the blade exists under the three water-depth conditions. Moreover, it can be observed that, under the three water-depth conditions, the maximum stress of the blade tends to decrease with the increase of water depth, but the maximum stress value is very close, so the change of water depth-conditions has little effect on the maximum stress of the blade under stable operation.

Figure 11 shows the variation of the average values of stress and deformation with the water depth during the stable operation of the turbine. It can be seen more directly that, as the water depth decreases, the average stress and average deformation of the blade show

an overall decreasing trend, and the average deformation of the blade does not change much after the water depth is lower than 0.6 m.

The influence of the tip-speed ratio (TSR) on the energy conversion of the turbine runner is relatively obvious. As the TSR increases, the runner thrust coefficient increases, and the thrust force acting on the blades also increases. Therefore, it is necessary to investigate the influence of TSR on the blade structure performance under the fluid–structure coupling condition and provide a theoretical basis for the blade strength design of tidal energy turbine. In this calculation, the incoming flow velocity of 0.4 m/s is kept constant, and the TSR is changed by changing the blade’s rotational speed. The rotational speeds are 92.69 r/min, 100 r/min, 102.11 r/min, and 110.01 r/min, respectively.

Figure 12 shows the graph of stress variation of the runner at different rotational speeds. When the turbine just started, the blade was also subjected to sudden load changes, and the maximum stress showed periodic fluctuations after 1 s. The higher the rotational speed, the greater the load acting on the blade. Take the rotation speed 100 r/min and 110.01 r/min for example; when the rotation speed increases by about 10%, the sudden stress on the blade at the initial start-up increases by about 30%. Therefore, in the designed operating speed range, the abrupt load changes generated at the start of the turbine cannot be ignored.

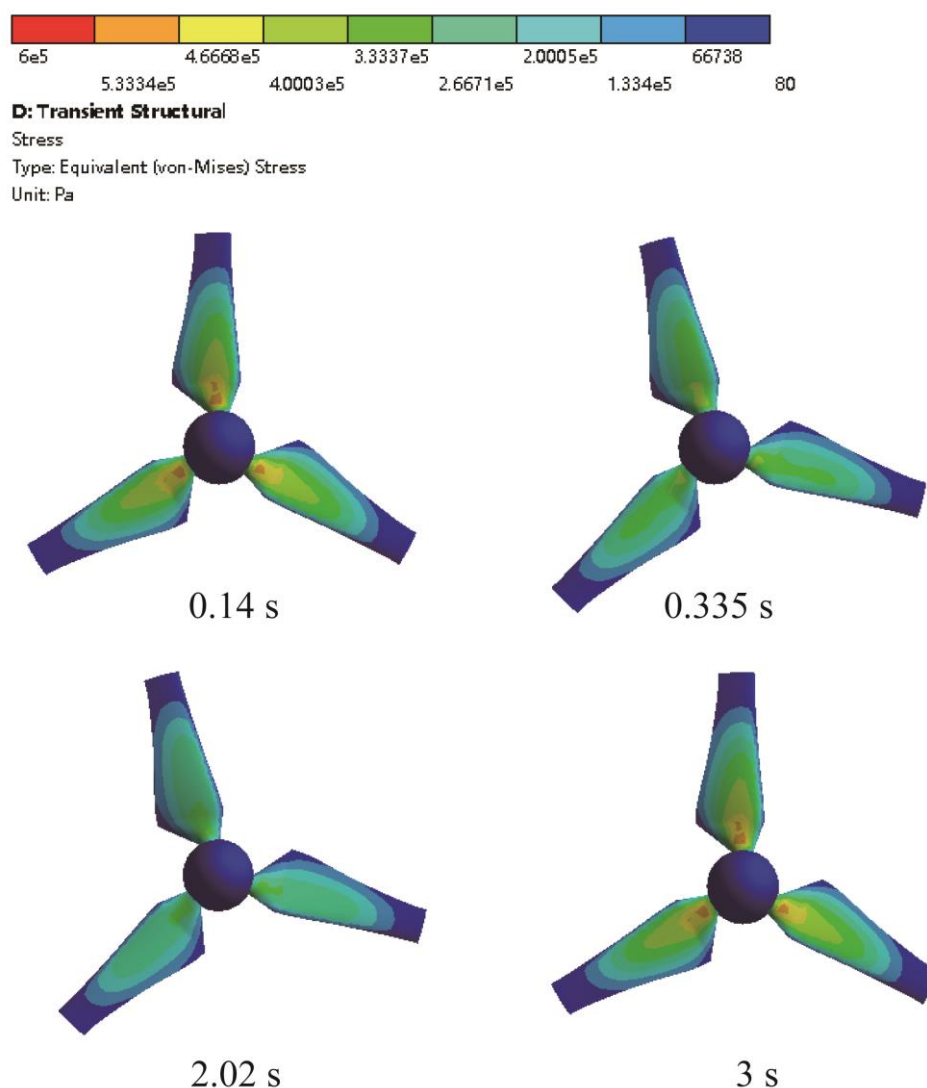


Figure 8. Distribution of blade’s dynamic stress at different times (Pa).

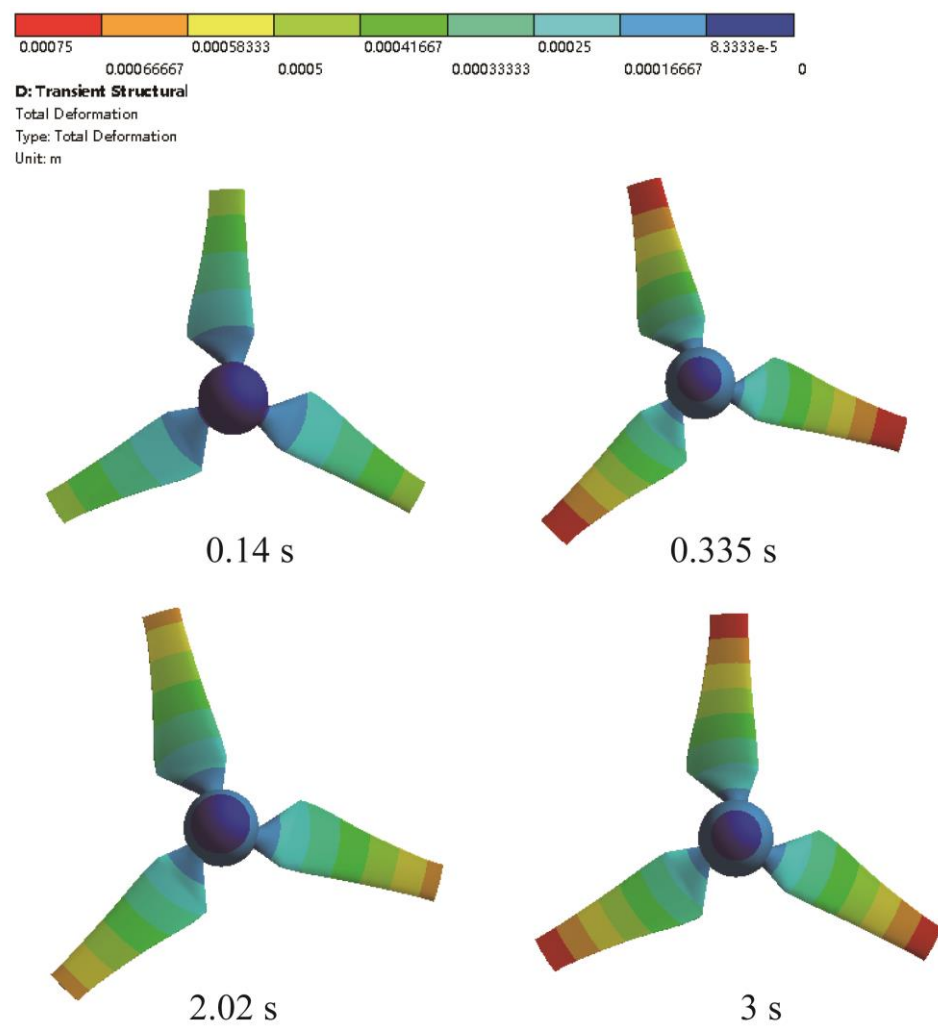


Figure 9. Distribution of blade deformation at different times (m).

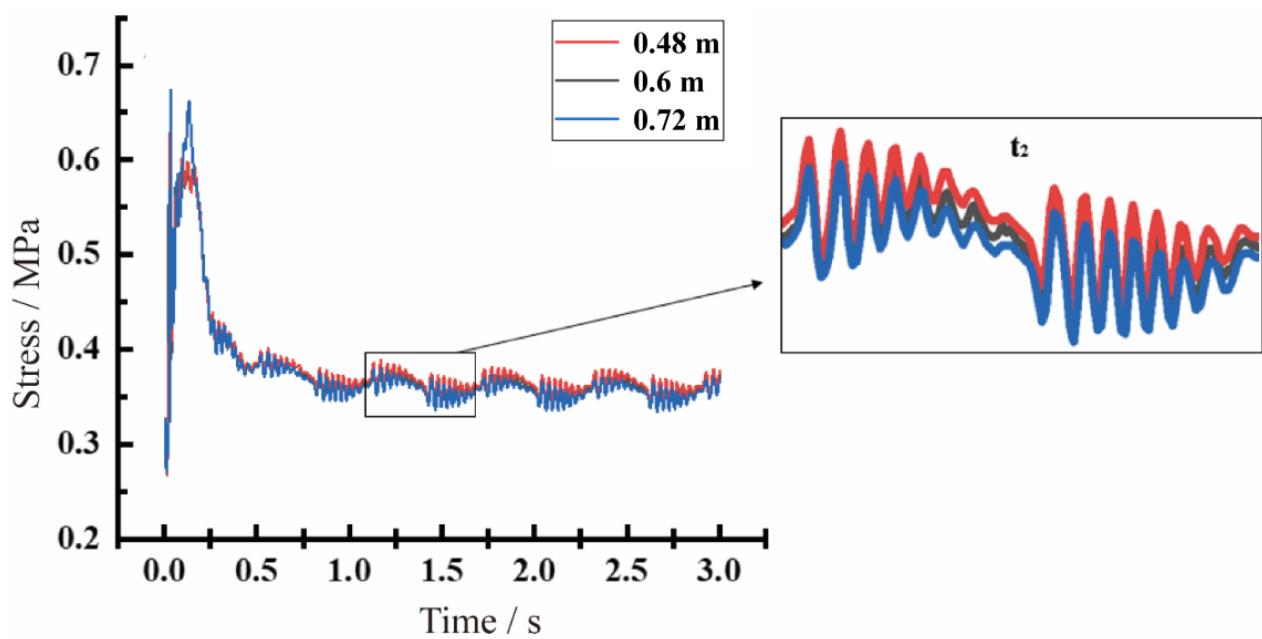


Figure 10. Variation of maximum stress of blade at different water depths.

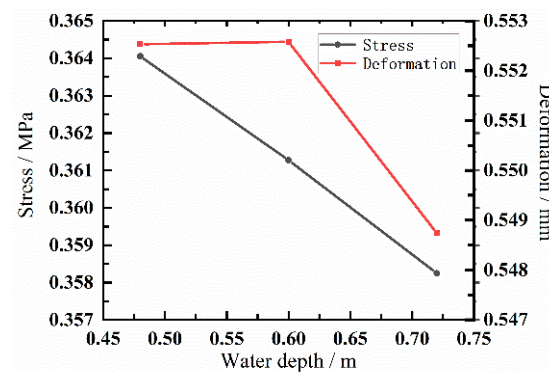


Figure 11. Stable cycle stress and deformation of the blade at different water depths.

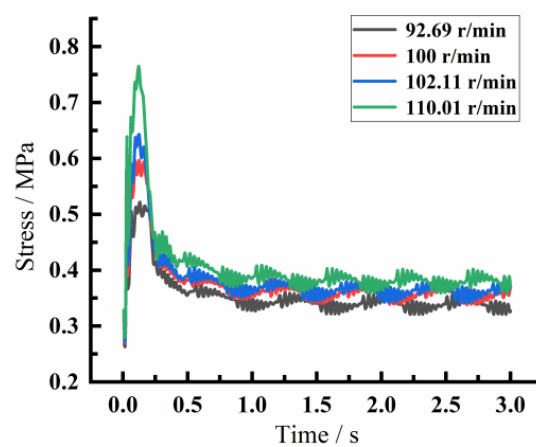


Figure 12. Variation of maximum blade stress at different rotation speeds.

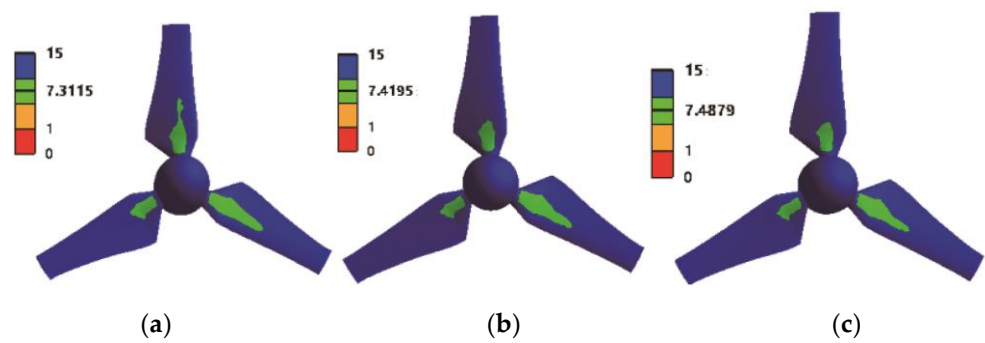
When the turbine operation was stabilized, the average stress and average deformation at four rotational speeds were calculated, as shown in Table 3. It can be found that the average stress and average deformation generally increase with the increase of rotational speed. The average stress becomes larger with the increase of the rotational speed, which is consistent with the trend of the thrust load on the blade. The stress and deformation of the blade are mainly caused by the fluid load [19], and the horizontal-axis tidal-energy turbine is mainly subjected to the axial-thrust force. Moreover, as the speed increases, the axial-thrust force on the turbine increases. The average deformation of the blade decreases at the maximum speed, and this may be due to the second-order oscillation of the blades.

Table 3. Average stress and average deformation.

Rotational Speed (r/min)	Average Stress (MPa)	Average Deformation (mm)
92.69	0.339	0.543
100	0.361	0.550
102.11	0.364	0.551
110.007	0.38	0.544

#### 4.3. Blade-Fatigue-Life Analysis

Figure 13 shows the distribution of the safety coefficient of the blade under different water-depth conditions. The safety factor is uniform, except in near the inner root section of the individual blades; it features irregular elliptical cores of the half safety factor extending along the blade's axis. The depth both slightly affects the distribution and increases the magnitude of the safety factor.



**Figure 13.** Blade safety factor at different water depths: (a) water depth of 0.48 m, (b) water depth of 0.6 m, and (c) water depth of 0.72 m.

Overall, the low safety coefficient of the blade is located at the root of the blade, which corresponds to the stress distribution of the blade in the previous section, where a large stress concentration occurs at the root of the blade leading to a decrease in the safety coefficient at the root. Meanwhile, with the increase of the water depth, the minimum safety coefficient increases slightly, but the influence range of the blade's minimum safety coefficient is basically the same under different water-depth conditions, and the influence range increases only under the minimum water depth.

Figure 14 depicts the safety-factor distribution of the blade under different TSR conditions. Individually (blade), the half-safety-factor area in the root stretches along the blade axis, though irregularly, with rotational speed. Figure 14d shows the distribution of the safety coefficients on the front and back of the blade at the maximum speed, and it is found that the range of the low safety coefficients on the back of the blade is much larger and has reached the middle of the blade. If the turbine is in a more complex marine environment, the middle of the blade may break, so special attention should be paid when performing the blade's strength calibration.

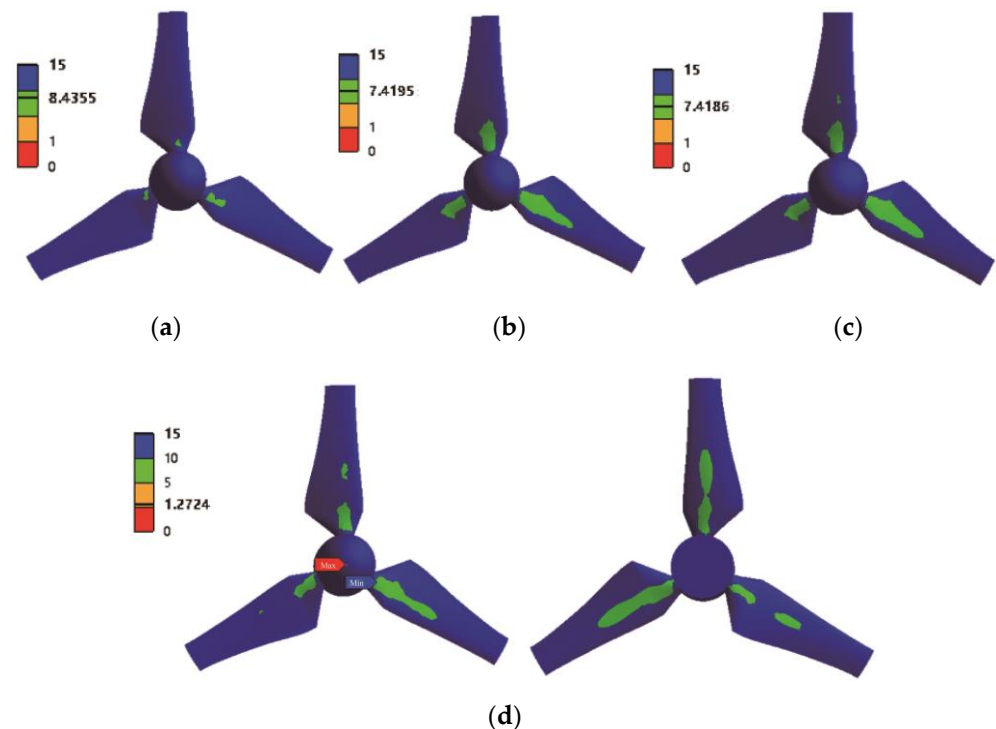


**Figure 14.** Blade safety factor at different rotational speeds: (a) 92.69 r/min, (b) 100 r/min, (c) 102.11 r/min, and (d) 110.01 r/min.



Considering the influence of different rotational speeds on the safety coefficient of the blade, the calculation of the number of stress cycles was carried out for different rotational speeds of the blade. The number of stress cycles of turbine blades under different rotational speeds all reach 108, indicating that the blades are in the safe range under these rotational speeds.

## 5. Conclusions

This paper calculated and analyzed the hydrodynamic performance and structural characteristics of the tidal stream turbine under bidirectional fluid–structure coupling conditions, and the main conclusions are as follows:

- (1) The difference between the calculated hydraulic turbine power coefficients with and without fluid–structure coupling conditions is not significant, and the deformation of the blade under the bidirectional fluid–structure coupling calculation will have a certain impact on the pressure difference on the blade’s surface.
- (2) As a cantilever beam structure, the blade has its maximum stress concentrated in the root of the leaf, and its maximum deformation is located near the tip of the leaf. The change of water depth has little influence on the stress and deformation of the blade, but the change of rotation speed has the most significant influence on it. The blade will be subjected to abrupt load when it is first started, and the increase of rotation speed will increase the abrupt load.
- (3) The fatigue-life prediction of the blade of the tidal-energy turbine was carried out. Similar to the blade stress variation, the lower safety factor of the blade is located near the root of the blade, and the blade’s rotation-speed variation has a more significant effect than water depth. The number of stress cycles of the blade at different rotational speeds is within the safety range.
- (4) During the design process of the blade, not only the hydraulic performance but also the strength of the blade situation should be taken into consideration.
- (5) These results represent an excellent initial step toward the wider use of the coupled fluid structure model due to high computational accuracy and resource efficiency; and toward further testing in more complex situations, such as incoming waves and currents, and floating turbine systems.

**Author Contributions:** Conceptualization, Y.Z. (Yuquan Zhang) and Z.L.; data curation, Z.L. and C.L.; funding acquisition, Y.Z. (Yuquan Zhang); investigation, Y.Z. (Yuquan Zhang) and X.W.; methodology, Y.Z. (Yuquan Zhang); resources, C.L.; supervision, Y.Z. (Yuan Zheng); validation, Z.L., X.W. and Z.Z.; writing—original draft, Y.Z. (Yuquan Zhang) and C.L.; writing—review and editing, X.W., Z.Z., E.F.-R., and R.J.M. All authors have read and agreed to the published version of the manuscript.

**Funding:** The research was supported by the following funding programs: National Natural Science Foundation of China (No. 52171257) and Natural Science Foundation of Jiangsu Province (No. BK20220144).

**Data Availability Statement:** Not applicable.

**Conflicts of Interest:** The authors declare that they have no known competing financial interests or personal relationships that could have appeared to influence the work reported in this paper.

## References

1. Zang, W.; Zheng, Y.; Zhang, Y.; Zhang, J.; Fernandez-Rodriguez, E. Experiments on the mean and integral characteristics of tidal turbine wake in the linear waves propagating with the current. *Ocean Eng.* **2019**, *173*, 1–11. [[CrossRef](#)]
2. Gaurier, B.; Ikhennecheu, M.; Germain, G.; Druault, P. Experimental study of bathymetry generated turbulence on tidal turbine behaviour. *Renew. Energy* **2020**, *156*, 1158–1170. [[CrossRef](#)]
3. Gaurier, B.; Carlier, C.; Germain, G.; Pinon, G.; Rivoalen, E. Three tidal turbines in interaction: An experimental study of turbulence intensity effects on wakes and turbine performance. *Renew. Energy* **2020**, *148*, 1150–1164. [[CrossRef](#)]
4. Derakhshan, S.; Ashoori, M.; Salemi, A. Experimental and numerical study of a vertical axis tidal turbine performance. *Ocean Eng.* **2017**, *137*, 59–67. [[CrossRef](#)]

5. Gaurier, B.; Druault, P.; Ikhennecheu, M.; Germain, G. Experimental analysis of the shear flow effect on tidal turbine blade root force from three-dimensional mean flow reconstruction. *Philos. Trans. R. Soc. A* **2020**, *378*, 20200001. [\[CrossRef\]](#)
6. Zhang, Y.; Zhang, J.; Lin, X.; Wang, R.; Zhang, C.; Zhao, J. Experimental investigation into downstream field of a horizontal axis tidal stream turbine supported by a mono pile. *Appl. Ocean Res.* **2020**, *101*, 102257. [\[CrossRef\]](#)
7. Zhang, Y.; Zhang, Z.; Zheng, J.; Zhang, J.; Zheng, Y.; Zang, W.; Lin, X.; Fernandez-Rodriguez, E. Experimental investigation into effects of boundary proximity and blockage on horizontal-axis tidal turbine wake. *Ocean Eng.* **2021**, *225*, 108829. [\[CrossRef\]](#)
8. Allmark, M.; Ellis, R.; Ebdon, T.; Lloyd, C.; Ordóñez-Sánchez, S.; Martínez, R.; Mason-Jones, A.; Johnstone, C.; O'Doherty, T. A detailed study of tidal turbine power production and dynamic loading under grid generated turbulence and turbine wake operation. *Renew. Energy* **2020**, *169*, 1422–1439. [\[CrossRef\]](#)
9. Myers, L.; Bahaj, A.S. Wake studies of a 1/30th scale horizontal axis marine current turbine. *Ocean. Eng.* **2005**, *34*, 758–762. [\[CrossRef\]](#)
10. Zhang, Y.; Zang, W.; Zheng, J.; Cappietti, L.; Zhang, J.; Zheng, Y.; Fernandez-Rodriguez, E. The influence of waves propagating with the current on the wake of a tidal stream turbine. *Appl. Energy* **2021**, *290*, 116729. [\[CrossRef\]](#)
11. Peng, B.; Zhang, Y.; Zheng, Y.; Wang, R.; Fernandez-Rodriguez, E.; Tang, Q.; Zhang, Z.; Zang, W. The effects of surge motion on the dynamics and wake characteristics of a floating tidal stream turbine under free surface condition. *Energy Convers. Manag.* **2022**, *266*, 115816. [\[CrossRef\]](#)
12. Tian, W.; VanZwieten, J.H.; Pyakurel, P.; Li, Y. Influences of yaw angle and turbulence intensity on the performance of a 20 kW in-stream hydrokinetic turbine. *Energy* **2016**, *111*, 104–116. [\[CrossRef\]](#)
13. Ahmadim, H.B.; Yang, Z. The evolution of turbulence characteristics in the wake of a horizontal axis tidal stream turbine. *Renew. Energy* **2020**, *151*, 1008–1015. [\[CrossRef\]](#)
14. Yazicioglu, H.; Tunc, K.M.; Ozbek, M.; Kara, T. Simulation of electricity generation by marine current turbines at Istanbul Bosphorus Strait. *Energy* **2016**, *95*, 41–50. [\[CrossRef\]](#)
15. Gonabadi, H.; Oila, A.; Yadav, A.; Bull, S. Fatigue life prediction of composite tidal turbine blades. *Ocean Eng.* **2022**, *260*, 111903. [\[CrossRef\]](#)
16. Finnegan, W.; Fagan, E.; Flanagan, T.; Doyle, A.; Goggins, J. Operational fatigue loading on tidal turbine blades using computational fluid dynamics. *Renew. Energy* **2020**, *152*, 430–440. [\[CrossRef\]](#)
17. Mullings, H.; Stallard, T. Assessment of Dependency of Unsteady Onset Flow and Resultant Tidal Turbine Fatigue Loads on Measurement Position at a Tidal Site. *Energies* **2021**, *14*, 5470. [\[CrossRef\]](#)
18. Bahaj, A.S.; Myers, L.E. Fundamentals applicable to the utilisation of marine current turbines for energy production. *Renew. Energy* **2003**, *28*, 2205–2211. [\[CrossRef\]](#)
19. Badshah, M.; Badshah, S.; Jan, S. Comparison of computational fluid dynamics and fluid structure interaction models for the performance prediction of tidal current turbines. *J. Ocean Eng. Sci.* **2020**, *5*, 164–172. [\[CrossRef\]](#)
20. Hafeez, N.; Badshah, S.; Badshah, M.; Khalil, S.J. Effect of velocity shear on the performance and structural response of a small-scale horizontal axis tidal turbine. *Mar. Syst. Ocean Technol.* **2019**, *14*, 51–58. [\[CrossRef\]](#)
21. Liu, X.F.; Wang, J.B.; Tian, M.L.; Tang, Z.B. Efficiency and Performance Analysis of Tidal Current Energy Turbine Basing on the Unidirectional Fluid-Structure Interaction. *Appl. Mech. Mater.* **2014**, *672*, 386–391. [\[CrossRef\]](#)
22. Ullah, H.; Hussain, M.; Abbas, N.; Ahmad, H.; Amer, M.; Noman, M. Numerical investigation of modal and fatigue performance of a horizontal axis tidal current turbine using fluid–structure interaction. *J. Ocean Eng. Sci.* **2019**, *4*, 328–337. [\[CrossRef\]](#)
23. Li, C.; Zheng, Y.; Zhang, Y.; Kan, K.; Xue, X.; Fernandez-Rodriguez, E. Stability Optimization and Analysis of a Bidirectional Shaft Extension Pump. *J. Fluids Eng.* **2020**, *142*. [\[CrossRef\]](#)
24. Khalid, S.-S.; Zhang, L.; Zhang, X.-W.; Sun, K. Three-dimensional numerical simulation of a vertical axis tidal turbine using the two-way fluid structure interaction approach. *J. Zhejiang Univ. Sci. Appl. Phys. Eng.* **2013**, *14*, 574–582. [\[CrossRef\]](#)
25. Badshah, M.; Badshah, S.; VanZwieten, J.; Jan, S.; Amir, M.; Malik, S.A. Coupled Fluid-Structure Interaction Modelling of Loads Variation and Fatigue Life of a Full-Scale Tidal Turbine under the Effect of Velocity Profile. *Energies* **2019**, *12*, 2217. [\[CrossRef\]](#)
26. Nicholls-Lee, R.F.; Turnock, S.R.; Boyd, S.W. Application of bend-twist coupled blades for horizontal axis tidal turbines. *Renew. Energy* **2013**, *50*, 541–550. [\[CrossRef\]](#)
27. Badshah, M.; Badshah, S.; Kadir, K. Fluid Structure Interaction Modelling of Tidal Turbine Performance and Structural Loads in a Velocity Shear Environment. *Energies* **2018**, *11*, 1837. [\[CrossRef\]](#)
28. Tatum, S.C.; Frost, C.H.; Allmark, M.; O'doherty, D.M.; Mason-Jones, A.; Prickett, P.W.; Grosvenor, R.I.; Byrne, C.B.; O'Doherty, T. Wave–current interaction effects on tidal stream turbine performance and loading characteristics. *Int. J. Mar. Energy* **2016**, *14*, 161–179. [\[CrossRef\]](#)